Lattice thermal conductivities of two SiO_2 polymorphs by first-principles calculations and the phonon Boltzmann transport equation

Keiyu Mizokami,[1] Atsushi Togo,[2,*] and Isao Tanaka[1,2,3]

[1]*Department of Materials Science and Engineering, Kyoto University, Sakyo, Kyoto 606-8501, Japan*
[2]*Center for Elements Strategy Initiative for Structural Materials, Kyoto University, Sakyo, Kyoto 606-8501, Japan*
[3]*Nanostructures Research Laboratory, Japan Fine Ceramics Center, Atsuta, Nagoya 456-8587, Japan*

(Received 10 April 2018; published 15 June 2018)

Lattice thermal conductivities of two SiO_2 polymorphs, i.e., α quartz (low) and α cristobalite (low), were studied using first-principles anharmonic phonon calculation and linearized phonon Boltzmann transport equation. Although α quartz and α cristobalite have similar phonon densities of states, phonon frequency dependencies of phonon group velocities and lifetimes are dissimilar, which results in largely different anisotropies of the lattice thermal conductivities. For α quartz and α cristobalite, distributions of the phonon lifetimes effective to determine the lattice thermal conductivities are well described by energy and momentum conservations of three phonon scatterings weighted by phonon occupation numbers and one parameter that represents the phonon-phonon interaction strengths.

DOI: 10.1103/PhysRevB.97.224306

I. INTRODUCTION

Recent computing power has enabled quantitative and systematic calculation of lattice thermal conductivity by using the combination of first-principles calculations and solutions of linearized phonon Boltzmann transport equation [1–19]. In this study, we applied this calculation to α quartz (low) and α cristobalite (low) of SiO_2. For the other polymorphs, the research on lattice thermal conductivity calculation of stishovite and $CaCl_2$-type SiO_2 in wide pressure and temperature ranges was reported by Aramberri *et al.* [20].

The α quartz and α cristobalite are the SiO_2 polymorphs. β cristobalite occurs at 1470 °C upon heating α quartz through the theoretical sequence of β quartz (573 °C) and β tridymite (870 °C) and turns into the metastable α-cristobalite phase upon cooling. High activation energy barrier between α quartz and α cristobalite prevents the transition from α cristobalite to α quartz so that they can exist at ordinary temperature and pressure. Crystal structures of α quartz and α cristobalite are shown in Fig. 1. The numbers of atoms in the unit cells (n_a) are 9 and 12, respectively. Both are made of SiO_4 tetrahedra connected by their vertices. Si atom is located at the center of each tetrahedron and O atoms are at the vertices.

The difference of these crystal structures is described by the patterns of the tetrahedron linkages. SiO_4 tetrahedra are more densely packed in α quartz. As a result, the volume per formula unit is more than ten percent smaller in α quartz. Their lattice parameters [21,22] are shown in Table II. Their space-group types are $P3_221$ (trigonal) for α quartz and $P4_12_12$ (tetragonal) for α cristobalite, by which both of them in principle have anisotropic thermal conductivity tensors with two independent elements, κ_{xx} and κ_{zz}. Although κ_{xx} and κ_{zz} of α quartz were reported [23], only its average value is known for α cristobalite [24].

The aim of this study is to understand their difference in lattice thermal conductivity. Indeed α quartz shows much larger anisotropy in lattice thermal conductivity than α cristobalite as presented in this study. This was investigated from microscopic properties due to phonons. By the long range interaction among atoms and softer low frequency phonon modes, we were required to conduct more careful calculations than we usually do in conjunction with our software development [25,26]. These computational details and comparisons of calculations with experiments are presented in Sec. II. Results of lattice thermal conductivity calculations and their analysis are presented in Sec. III. We show similarity and dissimilarity between α quartz and α cristobalite in mode contributions of lattice thermal conductivities and distributions of phonon properties as a function of phonon frequency. Then the characteristics of three phonon scatterings are discussed.

II. METHOD OF CALCULATION

A. Computational details

We solved linearized phonon Boltzmann transport equation with single-mode relaxation time approximation [15,27]. We abbreviate this approximation as RTA. For the phonon and lattice thermal conductivity calculations, we employed PHONOPY [28] and PHONO3PY [15] software packages. Unless specially denoted, q-point sampling meshes of $19 \times 19 \times 19$ and $19 \times 19 \times 14$ were used for the lattice thermal conductivity calculations of α quartz and α cristobalite, respectively. The isotope scattering effect calculated by the second-order perturbation theory [15,29] was found negligibly small at

*togo.atsushi@gmail.com

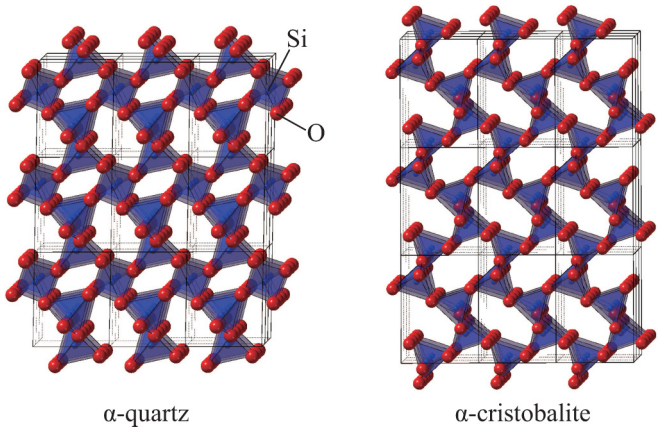

FIG. 1. Crystal structures of α quartz (left) and α cristobalite (right). The space-group types are $P3_221$ and $P4_12_12$, respectively.

300 K: 0.4% and 0.3% reductions in κ_{xx} and κ_{zz} of α quartz, respectively, and 0.3% and 0.1% reductions in κ_{xx} and κ_{zz} of α cristobalite, respectively. Therefore it was not included.

The experimental lattice parameters of α quartz [21] and α cristobalite [22] were used for all calculations in Sec. III. Choice of the lattice parameters can have a large impact to the lattice thermal conductivity since it is known that decreasing (increasing) lattice parameters increases (decreases) lattice thermal conductivity as has been well studied as pressure dependence of lattice thermal conductivity for many years [30–34]. In Sec. II B, we present calculated lattice thermal conductivity values obtained using experimental and calculated lattice parameters.

Second- and third-order force constants were calculated using the supercell approach with finite atomic displacements of 0.03 Å [15,35]. The supercells of $6 \times 6 \times 6$ (1944 atoms) and $4 \times 4 \times 4$ (768 atoms) of the unit cells were used for the calculations of the second-order force constants of α quartz and α cristobalite, respectively. Use of larger supercells is in general important to compute phonon-phonon scattering channels with better accuracy. For α quartz, it was necessary to take into account the long-range interaction to remove imaginary acoustic modes in the vicinity of Γ point. We expect real-space interaction range among three atoms effective for lattice thermal conductivity is relatively shorter than that of the second-order force constants. Therefore, for the third-order force constants, we chose $2 \times 2 \times 2$ supercells (72 and 96 atoms). Our supercell choices for α quartz and α cristobalite are considered reasonable after the examinations as presented in Sec. II B.

Running many supercell first-principles calculations for the third-order force constants is the most computationally demanding part throughout the lattice thermal conductivity calculation. To omit the computations of parts of force constants in some means, e.g., using real-space cutoff distance, can ease its total computational demand. However we filled all elements of the supercell force constants. Nevertheless our attempts and remarks on using the cutoff distance for computing third-order force constants, that we avoided, are presented in the Appendix.

Nonanalytical term correction [36–38] was applied to dynamical matrices to treat long range dipole-dipole interactions. Though impact of nonanalytical term correction to lattice thermal conductivity is often negligible for crystals containing a number of atoms in their unit cells such as α quartz (9 atoms) and α cristobalite (12 atoms), it turned out to be useful for α quartz to remove imaginary acoustic modes near Γ point in conjunction with using the larger supercell. This was achieved by the reciprocal space summation of dipole-dipole interaction contributions shown in Eq. (73) of Ref. [38] by Gonze and Lee although the simpler approach by Wang *et al.* [39] could not solve this problem.

For the first-principles calculations, we employed the plane-wave basis projector augmented wave method [40] within the framework of density functional theory (DFT) as implemented in the VASP code [41–43]. The generalized gradient approximation (GGA) of Perdew, Burke, and Ernzerhof revised for solids (PBEsol) [44] was used as the exchange correlation potential. A plane-wave energy cutoff of 520 eV was employed. The radial cutoffs of the PAW datasets of Si and O were 1.90 and 1.52 Å, respectively. The 3s and 3p electrons for Si and the 2s and 2p electrons for O were treated as valence and the remaining electrons were kept frozen. Reciprocal spaces of the α-quartz supercells used for the calculations of the third- and second-order force constants were sampled by the $3 \times 3 \times 3$ mesh and at only Γ point, respectively. The former mesh was shifted by a half grid distance in c^* direction from the Γ-point centered mesh. For the α-cristobalite supercells, the reciprocal spaces were sampled by the $2 \times 2 \times 2$ and $1 \times 1 \times 1$ meshes with half grid shifts along all three directions from the Γ-point centered meshes, respectively. To obtain atomic forces, the total energies were minimized until the energy convergences became less than 10^{-8} eV.

Static dielectric constant tensors and Born effective charge tensors were calculated from density functional perturbation theory as implemented in the VASP code [45,46]. These tensors were symmetrized by their space-group and crystallographic-point-group operations. A sum rule was applied to the Born effective charge tensors following Ref. [38]. For these calculations, the plane-wave cutoff energy of 600 eV was used. The reciprocal spaces of the α quartz and α cristobalite were sampled by the $12 \times 12 \times 12$ and $8 \times 8 \times 8$ k-point sampling meshes, respectively. The former mesh was shifted by a half grid distance along c^* direction and the later mesh was shifted by half grid distances along all three directions from the Γ-point centered meshes.

B. Choices of exchange correlation potentials and convergence criteria

We performed a series of lattice thermal conductivity calculations against different exchange correlation potentials, solutions of linearized phonon Boltzmann transport equation, and convergence criteria. We present our calculation results on them. After these examinations, we chose the calculation settings described in Sec. II A, which are considered to give results accurate enough for our discussion.

In Fig. 2, convergences of lattice thermal conductivities with respect to the number of sampling phonon modes in Brillouin zones are presented. For both α quartz and α cristobalite, the lattice thermal conductivities converge well by $\sim 10^5$ phonon-mode sampling points. Since we needed more

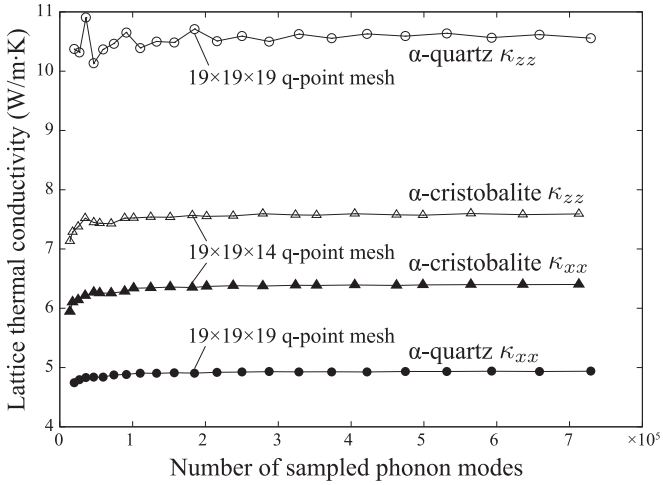

FIG. 2. Lattice thermal conductivities of α quartz and α cristobalite calculated at 300 K with different q-point sampling meshes using the PBEsol exchange correlation potential. Experimental lattice parameters were employed for these calculations. The lattice thermal conductivities are plotted as a function of a number of sampled phonon modes, i.e., product of a number of sampled q points and $3n_a$, where $n_a = 9$ for α quartz and $n_a = 12$ for α cristobalite.

sampling phonon modes to converge the curve shapes of spectrum-like plots such as phonon density of states (DOS), we chose the $19 \times 19 \times 19$ and $19 \times 19 \times 14$ q-point sampling meshes for α quartz and α cristobalite, respectively.

In Table I, experimental and calculated lattice thermal conductivities are presented. For the calculations, we employed RTA [15,27] and direct [11,15] solutions of linearized phonon Boltzmann transport equation, and the obtained values were close to each other for α quartz and α cristobalite. Therefore, we decided to use the RTA solution, since, compared with the direct solution, it has an advantage in analyzing results more easily and intuitively by its closed form of lattice thermal conductivity formula.

Due to crystal symmetries of α quartz (trigonal) and α cristobalite (tetragonal), both lattice thermal conductivity tensors have only two degrees of freedom, κ_{xx} and κ_{zz}. α quartz exhibits largely anisotropic lattice thermal conductivity whereas that of α cristobalite is more isotropic as shown in Table I. From the experimental measurement of α quartz by Kanamori *et al.* [23], the ratio κ_{zz}/κ_{xx} is around 2, which is well reproduced by our calculation. However the calculations of κ_{xx} and κ_{zz} underestimate the experimental values. There is another experimental measurement of powder sample reported by Kunugi *et al.* [24]. By taking $\kappa_{av} = (2\kappa_{xx} + \kappa_{zz})/3$ as an averaged value along orientations, the calculation underestimates the experiment. In the same report by Kunugi *et al.*, they also showed the measurement of powder α cristobalite, which is overestimated by the calculation. Since in this study, phonon-defect collisions are not considered for simplicity, calculations should tend to overestimate the experiments. In α cristobalite, many defects are created during the phase transition from the cubic β cristobalite to tetragonal α cristobalite upon cooling. Therefore it is reasonable that the calculation overestimates the experiment in α cristobalite. In α quartz, the calculation underestimates more than 20% relative to the experimental value by Kanamori *et al.* This absolute amount of error can occur depending on the choice of the exchange correlation potential or the lattice parameters, which are discussed below, however the fact that the calculation underestimates the experiments is unusual. We consider that DFT with these popular exchange correlation potentials such as PBEsol are difficult to predict the lattice thermal conductivity of α quartz as good as that can be achieved for a majority of other compounds. By the report by Linnera and Karttunen on Cu_2O, the use of PBE0 hybrid functional [47,48] with 25% Hartree-Fock and 75% PBE exchange improved the calculated lattice thermal conductivity compared with using PBE [47], where the former gave a roughly two times larger value than the latter [49]. Like this example, to obtain even better quantitative result, we probably need a better treatment of many body interaction of electrons although the qualitative result of α quartz would remain unchanged. In addition, the use of hybrid functionals is highly computationally demanding to apply to the lattice thermal conductivity calculation of α quartz and it is beyond our current computational resource. Therefore we employed the exchange correlation potential of PBEsol rather than a hybrid functional method.

It is not always the case that we can fortunately refer to experimental lattice parameters on lattice thermal conductivity calculations. Therefore it is of interest to see how much different lattice thermal conductivities are calculated using the lattice parameters determined by the first-principles calculations and those calculated with the experimental lattice parameters. In Table II, the experimental lattice parameters [21,22] of α quartz and α cristobalite and those optimized by calculations are presented. For the calculations, we employed the exchange correlation potentials of PBEsol, local density approximation (LDA) according to Ceperly and Alder as parameterized by Perdew and Zunger [50,51], and GGA in the Perdew-Burke-Ernzerhof form (PBE) [47]. Thermal expansion was not considered in the calculations. The calculated lattice parameters were underestimated by LDA and overestimated by PBEsol and PBE.

As shown in Table III, with the calculated lattice parameters, larger lattice thermal conductivities of α quartz and α

TABLE I. Experimental and calculated lattice thermal conductivities κ (W/m-K) of α quartz and α cristobalite at room temperature. In the calculations, RTA and direct solutions of linearized phonon Boltzmann transport equation are compared. Only the average values κ_{av} were given in the report by Kunugi *et al.* For the calculations and experiment by Kanamori *et al.*, we show average values, here simply defined as $\kappa_{av} = (2\kappa_{xx} + \kappa_{zz})/3$, to make rough comparisons.

		κ_{xx}	κ_{zz}	κ_{av}
α quartz	Expt. by Kanamori *et al.*[a]	6.49	13.9	8.97[c]
	Expt. by Kunugi *et al.*[b]			7.15
	RTA	4.9	10.7	6.8[c]
	Direct solution	5.1	10.9	7.0[c]
α cristobalite	Expt. by Kunugi *et al.*[b]			6.15
	RTA	6.4	7.6	6.8[c]
	Direct solution	6.6	7.2	6.8[c]

[a]Reference [23].
[b]Reference [24].
[c]$\kappa_{av} = (2\kappa_{xx} + \kappa_{zz})/3$.

TABLE II. Experimental and calculated lattice parameters of α quartz and α cristobalite. For the calculations, LDA, PBEsol, and PBE exchange correlation potentials were used and compared.

		a (Å)	c (Å)
α quartz	Expt.[a]	4.913	5.405
	Calc./LDA	4.873	5.374
	Calc./PBEsol	4.960	5.453
	Calc./PBE	5.028	5.518
α cristobalite	Expt.[b]	4.971	6.928
	Calc./LDA	4.956	6.887
	Calc./PBEsol	5.045	7.036
	Calc./PBE	5.092	7.114

[a]Reference [21].
[b]Reference [22].

cristobalite were obtained by the exchange correlation potentials that give smaller lattice parameters (Table II) following the general trend of the volume dependence, i.e., $\kappa_{\mathrm{LDA}} > \kappa_{\mathrm{PBEsol}} > \kappa_{\mathrm{PBE}}$ with $V_{0,\mathrm{LDA}} < V_{0,\mathrm{PBEsol}} < V_{0,\mathrm{PBE}}$, where V_0 is the volume of the unit cell. When using the experimental lattice parameters, the lattice thermal conductivities were calculated in the opposite order, $\kappa_{\mathrm{PBE}} > \kappa_{\mathrm{PBEsol}} > \kappa_{\mathrm{LDA}}$. From these calculations, we can see distinguishable effects by the choices of the exchange correlation potentials: One is in determining lattice parameters and the other is in calculating forces on atoms. However since the values and the ratios κ_{zz}/κ_{xx} in Table III are close enough, we consider that any choice given here is found a reasonable choice.

We investigated the effects on calculated lattice thermal conductivities by different choices of supercell size used for the calculation of the third-order force constants and finite atomic displacement distance and plane-wave cutoff energy used for the calculations of the second- and third-order force constants. The k points of the supercell reciprocal spaces were sampled with equivalent density meshes to those written in Sec. II A except for that of $3 \times 3 \times 2$ supercell of α cristobalite where the $2 \times 2 \times 2$ sampling mesh shifted in half grid distances along all directions from the Γ-point centered mesh was used.

TABLE III. Calculated lattice thermal conductivities κ (W/m-K) of α quartz and α cristobalite at 300 K with respect to the choices of lattice parameters (see Table II) and the exchange correlation potentials (XC func.) of PBEsol and LDA.

	Lattice params.	XC func.	κ_{xx}	κ_{zz}
α quartz	Calc./LDA	LDA	4.9	10.8
	Calc./PBEsol	PBEsol	4.2	8.7
	Calc./PBE	PBE	3.7	6.9
	Expt.	LDA	4.3	9.2
	Expt.	PBEsol	4.9	10.7
	Expt.	PBE	5.5	12.1
α cristobalite	Calc./LDA	LDA	5.7	6.6
	Calc./PBEsol	PBEsol	5.2	5.9
	Calc./PBE	PBE	5.2	5.8
	Expt.	LDA	5.3	6.1
	Expt.	PBEsol	6.4	7.6
	Expt.	PBE	7.2	8.7

TABLE IV. Calculated lattice thermal conductivities κ (W/m-K) of α quartz and α cristobalite at 300 K with respect to supercell size used to calculate third-order force constants and plane-wave energy cutoff (eV) and atomic displacement distance used to calculate second- and third-order force constants.

	Supercell	Displacement	PW cutoff	κ_{xx}	κ_{zz}
α quartz	$2 \times 2 \times 2$	0.03	520	4.9	10.7
	$3 \times 3 \times 2$	0.03	520	4.7	10.3
	$2 \times 2 \times 3$	0.03	520	4.7	10.5
	$1 \times 1 \times 1$	0.03	520	4.4	9.5
	$2 \times 2 \times 2$	0.03	600	5.0	10.8
	$2 \times 2 \times 2$	0.03	440	4.9	10.6
	$2 \times 2 \times 2$	0.01	520	5.1	11.0
	$2 \times 2 \times 2$	0.05	520	4.2	9.5
α cristobalite	$2 \times 2 \times 2$	0.03	520	6.4	7.6
	$3 \times 3 \times 2$	0.03	520	6.3	7.4
	$2 \times 2 \times 1$	0.03	520	5.7	6.6
	$1 \times 1 \times 1$	0.03	520	5.0	5.3
	$2 \times 2 \times 2$	0.01	520	6.4	7.6
	$2 \times 2 \times 2$	0.05	520	6.2	7.4

These results show, for both α quartz and α cristobalite, that $2 \times 2 \times 2$ supercells are the reasonable choices considering the tradeoff of convergences of the lattice thermal conductivity values and the required computational demands (see Appendix) with respect to our current computational resource. It also shows the use of the primitive unit cells for third-order force constants calculations is not a bad choice if a purpose is the rough estimation.

The choice of 0.05 Å displacement distance induces decrease of lattice thermal conductivity for α quartz. This is considered due to inclusion of higher order anharmonicity. In general, decreasing the displacement distance, numerical error in force constants is magnified. The results by the choice of 0.01 Å displacement distance give similar results with those by 0.03 Å. This means that the numerical errors and inclusions of higher order anharmonicity are managed to be small by the choice of 0.03 Å displacement distance for our computer simulation settings (Table IV).

III. RESULTS AND DISCUSSION

In RTA, lattice thermal conductivity κ is written in a closed form [27]:

$$\kappa = \frac{1}{N V_0} \sum_{\lambda} C_{\lambda} \mathbf{v}_{\lambda} \otimes \mathbf{v}_{\lambda} \tau_{\lambda}, \tag{1}$$

where N and V_0 are the number of unit cells in the system and volume of the unit cell, respectively. The suffix λ represents the phonon mode as the pair of phonon wave vector $\mathbf{q}$ and branch j, $\lambda \equiv (\mathbf{q}, j)$, and similarly we denote $-\lambda \equiv (-\mathbf{q}, j)$. C_{λ} is the mode heat capacity given as

$$C_{\lambda} = k_{\mathrm{B}} \left(\frac{\hbar \omega_{\lambda}}{k_{\mathrm{B}} T} \right)^2 \frac{\exp(\hbar \omega_{\lambda} / k_{\mathrm{B}} T)}{[\exp(\hbar \omega_{\lambda} / k_{\mathrm{B}} T) - 1]^2}, \tag{2}$$

where $\omega_{\lambda} = \omega(\mathbf{q}, j)$ is the phonon frequency, T is the temperature, and $\hbar$ and k_{B} denote the reduced Planck constant

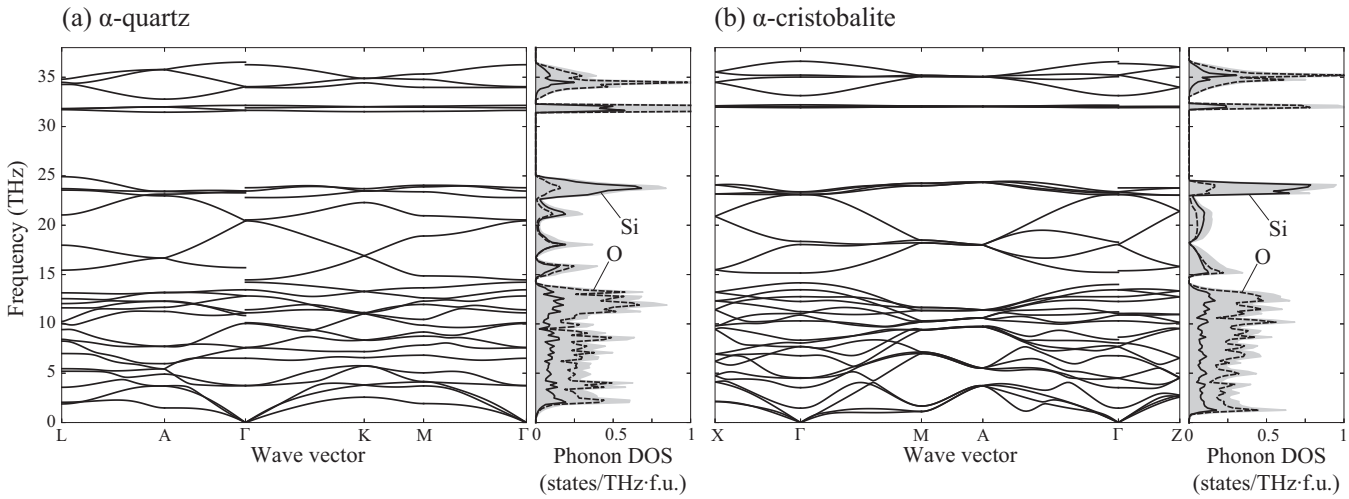

FIG. 3. Phonon band structures and DOS of (a) α quartz and (b) α cristobalite. In the DOS plots on the right hand sides of the band structures, the solid and dotted curves depict the partial DOS of Si and O, respectively, and the curves under shadow show the total DOS. The special point symbols of wave vectors follow the convention provided in the Bilbao crystallographic server [52].

and Boltzmann constant, respectively. $\mathbf{v}_\lambda$ is the phonon group velocity defined as the gradient of the phonon energy surface:

$$\mathbf{v}_\lambda = \nabla_{\mathbf{q}}\omega(\mathbf{q}, j). \tag{3}$$

τ_λ is the single-mode relaxation time and we use phonon lifetime as τ_λ. We calculated phonon lifetime $\tau_\lambda = \frac{1}{2\Gamma_\lambda(\omega_\lambda)}$ by [15,35]

$$\Gamma_\lambda(\omega) = \frac{18\pi}{\hbar^2}\sum_{\lambda'\lambda''}\Delta(-\mathbf{q}+\mathbf{q}'+\mathbf{q}'')N_{\lambda'\lambda''}(\omega)|\Phi_{-\lambda\lambda'\lambda''}|^2, \tag{4}$$

where

$$N_{\lambda'\lambda''}(\omega) = (n_{\lambda'}+n_{\lambda''}+1)\delta(\omega-\omega_{\lambda'}-\omega_{\lambda''}) + (n_{\lambda'}-n_{\lambda''}) \times [\delta(\omega+\omega_{\lambda'}-\omega_{\lambda''}) - \delta(\omega-\omega_{\lambda'}+\omega_{\lambda''})], \tag{5}$$

with $n_\lambda = [\exp(\hbar\omega_\lambda/k_BT)-1]^{-1}$ as the phonon occupation number at equilibrium. $\Phi_{\lambda\lambda'\lambda''}$ gives the phonon-phonon interaction strength among three phonons calculated from second- and third-order force constants. $\Delta(\mathbf{q}+\mathbf{q}'+\mathbf{q}'') \equiv 1$ if $\mathbf{q}+\mathbf{q}'+\mathbf{q}'' = \mathbf{G}$ otherwise 0, where $\mathbf{G}$ is the reciprocal lattice vector. This constraint comes from the lattice translational invariance that appears inside $\Phi_{\lambda\lambda'\lambda''}$ [15], however it is made visible in Eq. (4) for the analysis given below. More details such as the phase convention, coefficients, and $\Phi_{\lambda\lambda'\lambda''}$ are found in Ref. [15].

Phonon band structures and DOS of α quartz and α cristobalite are shown in Figs. 3(a) and 3(b), respectively. These phonon structures in their shapes show reasonable agreements with previous calculations and experiments reported in Refs. [37,53–57]. Between α quartz and α cristobalite, their total and partial DOS curves are analogous. In detail, the position of the first peak of α quartz from 0 THz is located at higher phonon frequency than that of α cristobalite. Their first peak positions roughly correspond to M and L points of α quartz and M point of α cristobalite in respective phonon band structures. These low phonon modes are considered to be made of rigid unit motions of SiO_4 tetrahedra [58–60], i.e., the phonon band structures at low frequencies reflect the different styles of the tetrahedron linkages.

To visualize phonon mode contribution to lattice thermal conductivity, we define $\kappa(\omega)$ as

$$\kappa(\omega) \equiv \frac{1}{NV_0}\sum_\lambda C_\lambda \mathbf{v}_\lambda \otimes \mathbf{v}_\lambda \tau_\lambda \delta(\omega-\omega_\lambda) \tag{6}$$

to be

$$\kappa = \int_0^\infty \kappa(\omega)d\omega. \tag{7}$$

Compared with phonon DOS written as $1/N\sum_\lambda \delta(\omega-\omega_\lambda)$, Eq. (6) is considered as a weighted DOS and each weight $C_\lambda \mathbf{v}_\lambda \otimes \mathbf{v}_\lambda \tau_\lambda / V_0$ is understood as a microscopic contribution of phonon mode λ to lattice thermal conductivity at ω_λ. In Fig. 4(a), $\kappa(\omega)$ of α quartz and α cristobalite are drawn as a function of phonon frequency at 300 K. We can see large peaks below 5 THz, where the phonon modes determine more than 50% of κ_{xx} and κ_{zz} of α quartz and α cristobalite. The curve shapes of $\kappa(\omega)$ are similar to those of the phonon DOS below their first peaks. Therefore it is considered that the number of states is the dominating factor of the lattice thermal conductivities in these phonon frequency ranges. Above 5 THz, $\kappa(\omega)$ are relatively small, however they contribute little by little to κ up to ~25 THz.

Anisotropy of lattice thermal conductivity, i.e., the ratio κ_{zz}/κ_{xx}, is larger in α quartz than in α cristobalite. The phonon mode contributions to the anisotropic κ are discussed using cumulative lattice thermal conductivity given by

$$\kappa^c(\omega) = \int_0^\omega \kappa(\omega')d\omega'. \tag{8}$$

Obviously $\lim_{\omega\to\infty}\kappa^c(\omega) = \kappa$ from Eq. (7). The ratios $\kappa^c_{zz}(\omega)/\kappa^c_{xx}(\omega)$ are shown in Fig. 5, where α quartz and α cristobalite present similar behaviors, although their intensities are different. Increasing phonon frequency from 0 THz, their ratios rapidly increase at low phonon frequencies and start to decrease gently until the ratios become κ_{zz}/κ_{xx}. This difference is exhibited in distributions of $\mathbf{v}_\lambda \otimes \mathbf{v}_\lambda$ that are written in

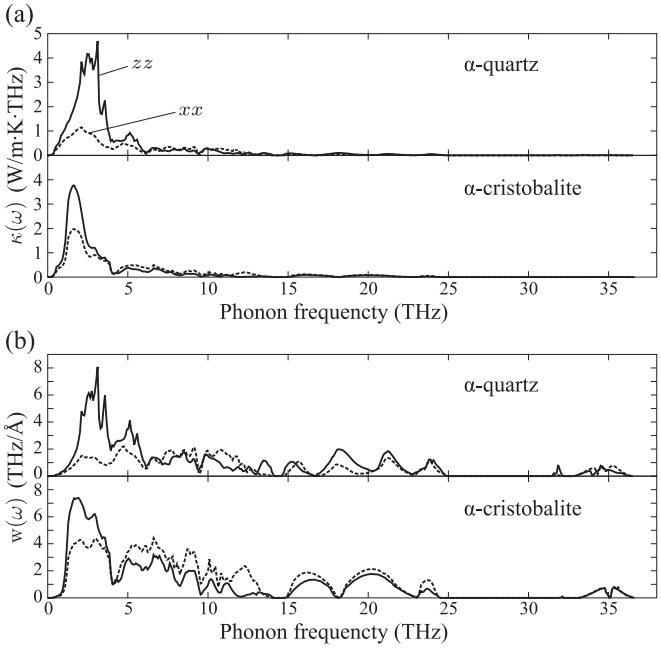

FIG. 4. (a) Mode contributions of lattice thermal conductivities $\kappa(\omega)$ at 300 K and (b) distributions of direct-vector-products of group velocities $\mathrm{w}(\omega)$ [see Eq. (9)] calculated for α quartz and α cristobalite with respect to phonon frequency. Both in (a) and (b), dotted and solid curves depict their xx and zz components, respectively.

analogy to $\kappa(\omega)$ of Eq. (6) as

$$\mathrm{w}(\omega) \equiv \frac{1}{NV_0} \sum_{\lambda} \mathbf{v}_\lambda \otimes \mathbf{v}_\lambda \delta(\omega - \omega_\lambda). \tag{9}$$

$\mathrm{w}(\omega)$ are shown in Fig. 4(b). Below 5 THz, the ratio between $\mathrm{w}_{zz}(\omega)$ and $\mathrm{w}_{xx}(\omega)$ is clearly larger in α quartz than in α cristobalite.

Comparing Figs. 4(a) and 4(b), increasing phonon frequency, $\kappa(\omega)$ more quickly decrease after first large peaks than $\mathrm{w}(\omega)$ in both α quartz and α cristobalite. This is due to phonon frequency dependencies of $C_\lambda \tau_\lambda$, however the effect of C_λ to the curve shapes of $\kappa(\omega)$ with respect to those of $\mathrm{w}(\omega)$ is small since C_λ is approximately constant $\sim k_\mathrm{B}$ at 300 K below 10 THz. In Fig. 6, τ_λ are plotted by dots as a function of phonon frequency. Increasing phonon frequency from 0 THz, the phonon lifetimes decrease quickly and then keep roughly constant with relatively small values. Both α quartz and α cristobalite show the same trend but with different rate of decrease, which clearly impacts the shapes of $\kappa(\omega)$ in Fig. 4(a), e.g., $\kappa(\omega)$ of α cristobalite corresponding to the second peak of $\mathrm{w}(\omega)$ at $\sim$3 THz is removed by the decrease of τ_λ.

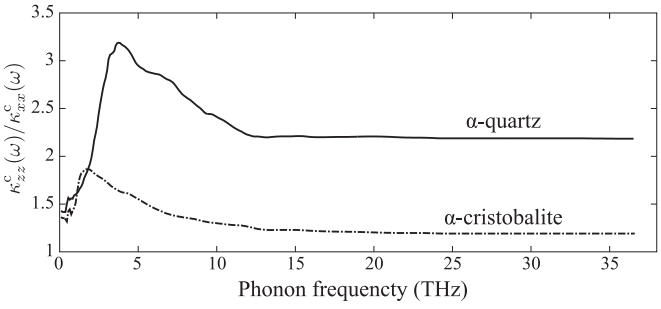

FIG. 5. Ratios between zz and xx elements of cumulative lattice thermal conductivities, $\kappa^\mathrm{c}_{zz}(\omega)/\kappa^\mathrm{c}_{xx}(\omega)$, in α quartz (solid curve) and α cristobalite (dashed-dotted curve) at 300 K.

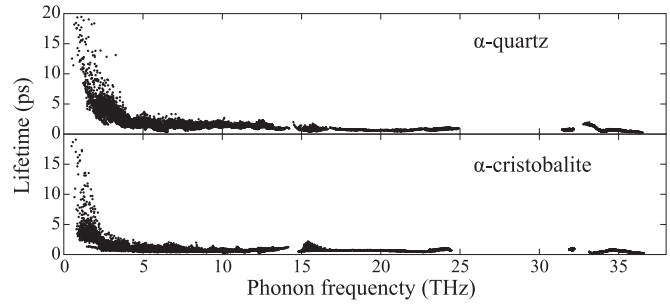

FIG. 6. Phonon lifetimes of α quartz and α cristobalite at 300 K with respect to phonon frequency. Each dot corresponds to one phonon mode. The points are sampled on the $19 \times 19 \times 19$ mesh for α quartz and $19 \times 19 \times 14$ mesh for α cristobalite in the respective Brillouin zones.

Recalling Eq. (4), τ_λ is constructed from the wave vector constraint $\Delta(\mathbf{q} + \mathbf{q}' + \mathbf{q}'')$, weighted energy conservation $N_{\lambda'\lambda''}(\omega_\lambda)$, and $|\Phi_{\lambda\lambda'\lambda''}|^2$. To make our discussion simple, we replace $|\Phi_{\lambda\lambda'\lambda''}|^2$ by a constant value $\tilde{P}$ if $\mathbf{q} + \mathbf{q}' + \mathbf{q}'' = \mathbf{G}$ or by 0 otherwise. As an attempt, we use $\tilde{P} = \tilde{P}_\mathrm{av}$ defined as an average of $|\Phi_{\lambda\lambda'\lambda''}|^2$ by

$$\tilde{P}_\mathrm{av} \equiv \frac{1}{(3n_\mathrm{a})^3 N^2} \sum_{\lambda\lambda'\lambda''} |\Phi_{\lambda\lambda'\lambda''}|^2 = \frac{1}{3n_\mathrm{a} N^2} \sum_{\lambda} P_\lambda, \tag{10}$$

where P_λ is that for one phonon mode [15]:

$$P_\lambda \equiv \frac{1}{(3n_\mathrm{a})^2} \sum_{\lambda'\lambda''} |\Phi_{\lambda\lambda'\lambda''}|^2. \tag{11}$$

Since $(3n_\mathrm{a})^2 N \tilde{P}_\mathrm{av}$ of α quartz and α cristobalite give the equivalent values as shown in Table V, we expect that they have similar phonon-phonon interaction strengths.

With $\tilde{P}$, $\Gamma_\lambda(\omega)$ is reduced to

$$\tilde{\Gamma}_\lambda(\omega) = \frac{18\pi}{\hbar^2} \tilde{P} \sum_{\lambda'\lambda''} \Delta(-\mathbf{q} + \mathbf{q}' + \mathbf{q}'') N_{\lambda'\lambda''}(\omega). \tag{12}$$

In Eq. (12), the summation on the right hand side is made of three phonon scattering channels weighted by phonon occupation numbers, which can be computed from the second-order force constants. The lattice thermal conductivities calculated with $\tilde{P} = \tilde{P}_\mathrm{av}$ and $\tilde{\tau}_\lambda = (2\tilde{\Gamma}_\lambda)^{-1}$, that we denote $\tilde{\kappa}$, are presented in Table V. These values are one order of magnitude smaller than the values in Table I, however the anisotropies

TABLE V. $\tilde{P}_\mathrm{av}$ (meV^2) [see Eq. (10)] and lattice thermal conductivities $\tilde{\kappa}$ (W/m-K) of α quartz and α cristobalite calculated using $\tilde{P}_\mathrm{av}$ at 300 K. To align the scale of $\tilde{P}_\mathrm{av}$ between α quartz and α cristobalite, $(3n_\mathrm{a})^2 N$ are multiplied with corresponding $\tilde{P}_\mathrm{av}$, where $n_\mathrm{a} = 9$ and $N = 19 \times 19 \times 19$ for α quartz and $n_\mathrm{a} = 12$ and $N = 19 \times 19 \times 14$ for α cristobalite.

	$(3n_\mathrm{a})^2 N \tilde{P}_\mathrm{av}$	$\tilde{\kappa}_{xx}$	$\tilde{\kappa}_{zz}$
α quartz	2.67	0.54	1.16
α cristobalite	2.78	1.00	1.17

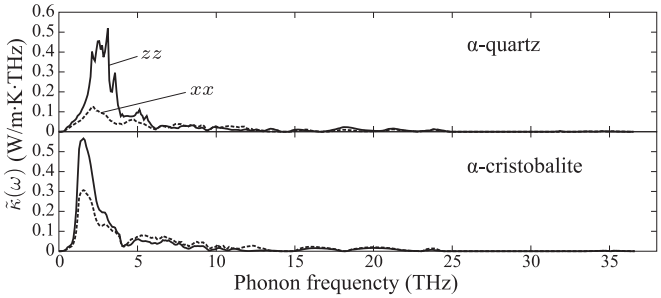

FIG. 7. $\tilde{\kappa}(\omega)$, mode contributions of lattice thermal conductivities of α quartz and α cristobalite calculated with $\tilde{P} = \tilde{P}_{\rm av}$ at 300 K as a function of phonon frequency. Dotted and solid curves depict $\tilde{\kappa}_{xx}$ and $\tilde{\kappa}_{zz}$, respectively.

$\tilde{\kappa}_{zz}/\tilde{\kappa}_{xx}$ are well reproduced, and as shown in Fig. 7, the curve shapes of the mode contributions of lattice thermal conductivities, denoted by $\tilde{\kappa}(\omega)$, are almost identical to those of $\kappa(\omega)$ presented in Fig. 4(a).

In Fig. 8, P_λ of α quartz and α cristobalite are plotted as a function of phonon frequency. Their distributions are similar except at low phonon frequency domains where the phonon DOS are small, which indicates that the different styles of linkages of SiO_4 tetrahedra in their crystal structures impact little to determine the phonon-phonon interaction strengths. In Fig. 8, there are four characteristic phonon frequency domains. The locations of these domains synchronize with the phonon DOS shown in Figs. 3(a) and 3(b). Between 0 to 15 THz, P_λ are roughly constant, by which, apart from their different magnitudes, similar phonon frequency dependencies of $\tilde{\tau}_\lambda$ to those of τ_λ are obtained as shown in Fig. 9. This enables the curve shapes of $\tilde{\kappa}(\omega)$ to become equivalent to those of $\kappa(\omega)$. Since more than 90% of the lattice thermal conductivities of α quartz and α cristobalite are recovered in $\kappa(\omega)$ below 15 THz, having a good estimate of the constant value, e.g., $\tilde{P} \sim \tilde{P}_{\rm av} \times 10^{-1}$, it is considered possible to predict the lattice thermal conductivities without computing third order force constants. P_λ start to increase from ~15 THz to the phonon band gap at ~25 THz. The two small domains above 30 THz correspond to respective two localized phonon bands. The ratio of Si and O partial DOS gradually increases by increasing phonon frequency below 15 THz. This represents that SiO_4 rigid

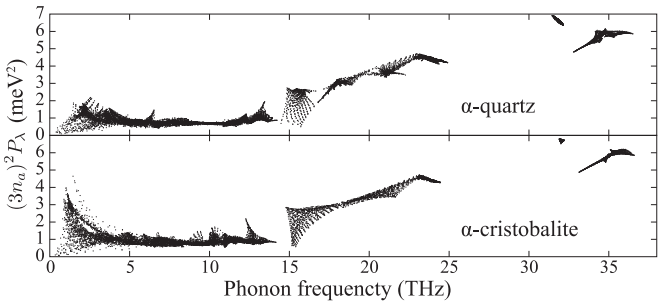

FIG. 8. $(3n_{\rm a})^2 P_\lambda$ of α quartz and α cristobalite with respect to phonon frequency. Here $(3n_{\rm a})^2$ is multiplied with P_λ to align the scale between α quartz and α cristobalite. Each dot corresponds to one phonon mode. The points are sampled on the $19 \times 19 \times 19$ mesh for α quartz and $19 \times 19 \times 14$ mesh for α cristobalite in the respective Brillouin zones.

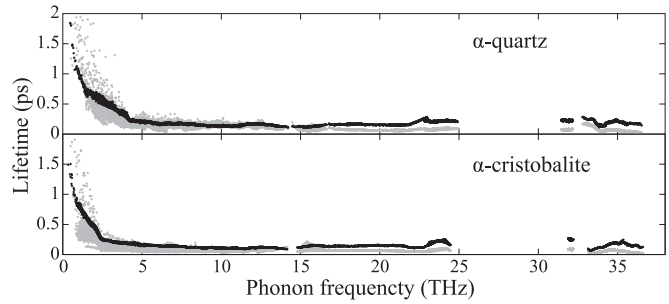

FIG. 9. $\tilde{\tau}_\lambda$, phonon lifetimes of α quartz and α cristobalite calculated with $\tilde{P} = \tilde{P}_{\rm av}$ at 300 K as a function of phonon frequency (black dots). To compare, $\tau_\lambda \times 10^{-1}$ (Fig. 6) are shown as the gray dots behind the black dots. The points are sampled on the $19 \times 19 \times 19$ mesh for α quartz and $19 \times 19 \times 14$ mesh for α cristobalite in the respective Brillouin zones.

units vibrate translationally at lower phonon frequencies and rotationally at increasing phonon frequencies. Above 15 THz, it is considered that the larger P_λ, i.e., larger anharmonicity, arises due to phonons that distort SiO_4 tetrahedron units.

IV. SUMMARY

The lattice thermal conductivity calculations were performed for α quartz and α cristobalite using first-principles anharmonic phonon calculation and linearized phonon Boltzmann transport equation. Since direct and RTA solutions gave similar values of the lattice thermal conductivities that also agree well with the experimental values, we focused on our discussion using the RTA solutions and phonon frequency dependencies of the phonon properties. The mode contributions of the lattice thermal conductivities $\kappa(\omega)$ show the characteristic differences of phonon mode contributions to the lattice thermal conductivities between α quartz and α cristobalite. Below 2 THz for α cristobalite and 3 THz for α quartz, phonon DOS and $\mathbf{v}_\lambda \otimes \mathbf{v}_\lambda$ determines the shapes of $\kappa(\omega)$. Above 5 THz, $\kappa(\omega)$ becomes much smaller than those below 5 THz following the phonon frequency dependence of τ_λ. The large difference of anisotropies in the lattice thermal conductivities of α quartz and α cristobalite was found. This is mainly attributed by the distributions of the phonon group velocities below 5 THz. The distributions of the phonon lifetimes effective to determine the lattice thermal conductivities around room temperature were well described by the momentum conservation $\Delta(\mathbf{q} + \mathbf{q}' + \mathbf{q}'')$, the energy conservation weighted by the phonon occupation numbers $N_{\lambda'\lambda''}(\omega_\lambda)$, and a parameter $\tilde{P}$ that represents the phonon-phonon interaction strengths.

ACKNOWLEDGMENTS

This work was supported by Grant-in-Aid for Scientific Research on Innovative Areas "Nano Informatics" (Grant No. 25106005) from the Japan Society for the Promotion of Science (JSPS), and by MEXT Japan through ESISM (Elements Strategy Initiative for Structural Materials) of Kyoto University.

APPENDIX: EFFECT OF USING REAL-SPACE CUTOFF TO CALCULATE SUPERCELL THIRD-ORDER FORCE CONSTANTS

Use of real-space cutoff distance to compute third-order force constants in the supercell approach may drastically reduce computational demand of lattice thermal conductivity calculation. However it should be used carefully since the side effect such as degradation of the numerical quality has not been well understood. In this Appendix, we provide our examinations on the effect of using a cutoff distance for the third-order force constants calculations. There are many possible ways to cut off third-order force constants. Below, we explain our scheme and show the convergence analysis.

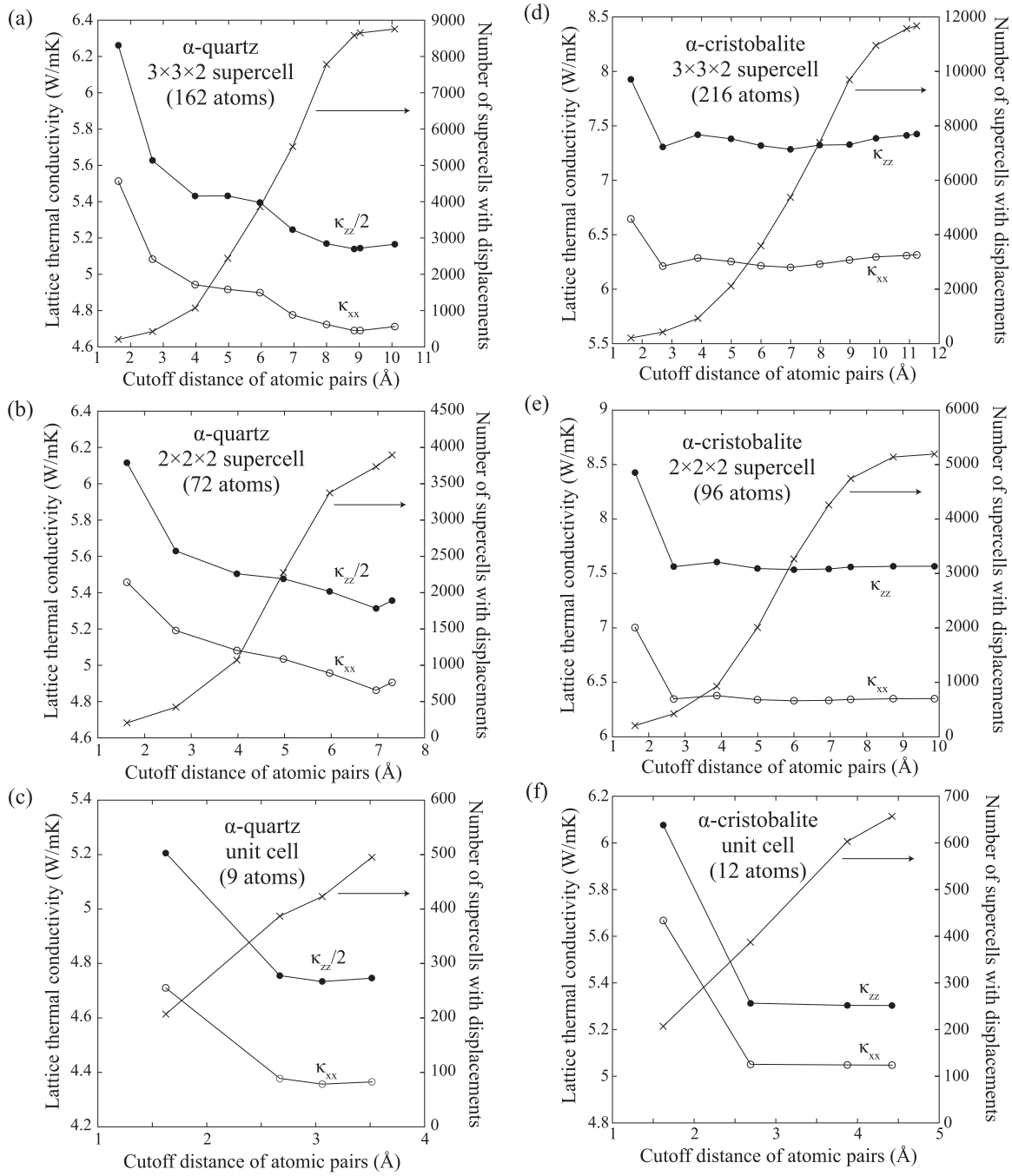

FIG. 10. Lattice thermal conductivities at 300 K with respect to cutoff distances of atomic pairs used to compute third-order force constants employing (a) α-quartz $3 \times 3 \times 2$ supercell (162 atoms), (b) α-quartz $2 \times 2 \times 2$ supercell (72 atoms), (c) α-quartz unit cell (9 atoms), (d) α-cristobalite $3 \times 3 \times 2$ supercell (216 atoms), (e) α-cristobalite $2 \times 2 \times 2$ supercell (96 atoms), and (f) α-cristobalite unit cell (12 atoms). The selected cutoff distances are those closest to but below (a) 2, . . . ,11 Å, (b) 2, . . . ,8 Å, (c) 2, 3, 3.5, and 4 Å, (d) 2, . . . ,12 Å, (e) 2, . . . ,10 Å, and (f) 2, . . . ,5 Å, respectively. The filled circles depict $\kappa_{zz}/2$ for α quartz and κ_{zz} for α cristobalite, and the open circles show κ_{xx}. The cross symbols present the numbers of supercells with displacements that were used to compute the third-order force constants with the respective cutoff distances. The rightmost points correspond to the results obtained without using the cutoff distances. Lines are eye guides.

1. Scheme

We calculate supercell third-order force constant element from two atomic displacements and a force on an atom by [15],

$$\Phi_{\alpha\beta\gamma}(l\kappa,l'\kappa',l''\kappa'') \simeq -\frac{F_\gamma[l''\kappa''; \mathbf{u}(l\kappa),\mathbf{u}(l'\kappa')]}{u_\alpha(l\kappa)u_\beta(l'\kappa')}, \quad \text{(A1)}$$

where $u_\alpha(l\kappa)$ means the finite displacement of the atom at the position $\mathbf{r}(l\kappa)$ along the αth Cartesian axis. The indices l and κ denote the lattice point and the atom in the unit cell, respectively. $F_\gamma[l''\kappa''; \mathbf{u}(l\kappa),\mathbf{u}(l'\kappa')]$ gives the force that the atom $l''\kappa''$ experiences by two atomic displacements $\mathbf{u}(l\kappa)$ and $\mathbf{u}(l'\kappa')$. Here it is assumed that we can obtain forces on all atoms in the supercell at once by each supercell calculation with a pair of atomic displacements. This assumption is currently normal in the DFT calculations since the computation of forces from existing electronic wave function requires relatively small computation.

Our cutoff distance R_{cut} is used to collect all the displaced atomic pairs whose distances $\sqrt{|\mathbf{r}(l\kappa) - \mathbf{r}(l'\kappa')|^2}$ are shorter than R_{cut}. The set of these pair displacements fills all supercell third-order force constant elements except for the elements whose three atoms are mutually more distant than R_{cut}.

2. Results

In this section, we present calculated lattice thermal conductivities using different cutoff distances and see the convergences in α quartz and α cristobalite using different supercell sizes. We employed $3 \times 3 \times 2$ and $2 \times 2 \times 2$ supercells and unit cells for these examinations. The computations of third-order force constants using the $3 \times 3 \times 2$ supercells were computationally very demanding for our current computational resource to fill all the elements, but not with the $2 \times 2 \times 2$. For α quartz, one $3 \times 3 \times 2$ supercell calculation was five times more computationally demanding than one $2 \times 2 \times 2$ supercell calculation. For α cristobalite, that was nine times because of the denser k-point sampling for the $3 \times 3 \times 2$ supercell calculation of α cristobalite.

The purpose to use the cutoff distance is to obtain accurate third-order force constants with reasonable computational demand though it is safer to compute all elements of supercell force constants to avoid a sudden cut of those elements since it is difficult to predict what happens after Fourier transformation of the third-order force constants with the cut.

In Figs. 10(a), 10(b) and 10(c), the lattice thermal conductivities of α quartz calculated against the cutoff distances are shown for three different supercell sizes. The lattice thermal conductivities generally decrease increasing the cutoff distance in these supercell sizes. It looks that each lattice thermal conductivity converges toward its rightmost point that corresponds to the full calculation where all elements of the supercell third-order force constants were filled. In Fig. 10(b), at the rightmost point, the lattice thermal conductivity increases in contradiction to the tendency of decreasing with increasing the cutoff distance. This is considered a visible effect of the cut of the supercell third-order force constants elements. For α cristobalite as shown in Figs. 10(d), 10(e) and 10(f), the convergence is achieved at relatively shorter cutoff distance of ~4 Å. This is about the distance between two atoms in neighboring SiO_4 tetrahedra. However the calculation of the third-order force constants with the $3 \times 3 \times 2$ supercell using ~4 Å cutoff distance is already more computationally demanding than the full calculation with the $2 \times 2 \times 2$ supercell. Therefore the supercell size has to be chosen systematically along with the choice of the cutoff distance. Comparing Figs. 10(a) and 10(d), we can see lattice thermal conductivity of α cristobalite converges more quickly than that of α quartz. For α quartz, it is difficult to define the convergence criterion to choose the cutoff distance for the accurate lattice thermal conductivity calculation.

For a purpose of the rough estimation, any choice of the cutoff distance and supercell size seems acceptable in the present case of α quartz and α cristobalite. In these SiO_2 polymorphs, the first nearest neighbor distance is well isolated because of SiO_4 tetrahedra. This may be the reason why the atomic interaction range effective to determine lattice thermal conductivity is found to be short.

[1] R. Peierls, Ann. Phys. **395**, 1055 (1929).
[2] R. Peierls, Ann. Inst. Henri Poincare **5**, 177 (1935).
[3] R. J. Hardy, Phys. Rev. B **2**, 1193 (1970).
[4] M. Omini and A. Sparavigna, Il Nuovo Cimento D **141**, 1537 (1997).
[5] G. Deinzer, G. Birner, and D. Strauch, Phys. Rev. B **67**, 144304 (2003).
[6] D. A. Broido, A. Ward, and N. Mingo, Phys. Rev. B **72**, 014308 (2005).
[7] D. A. Broido, M. Malorny, G. Birner, N. Mingo, and D. A. Stewart, Appl. Phys. Lett. **91**, 231922 (2007).
[8] A. Ward, D. A. Broido, D. A. Stewart, and G. Deinzer, Phys. Rev. B **80**, 125203 (2009).
[9] J. E. Turney, E. S. Landry, A. J. H. McGaughey, and C. H. Amon, Phys. Rev. B **79**, 064301 (2009).
[10] A. Chernatynskiy and S. R. Phillpot, Phys. Rev. B **82**, 134301 (2010).
[11] L. Chaput, Phys. Rev. Lett. **110**, 265506 (2013).
[12] G. Fugallo, M. Lazzeri, L. Paulatto, and F. Mauri, Phys. Rev. B **88**, 045430 (2013).
[13] O. Hellman and D. A. Broido, Phys. Rev. B **90**, 134309 (2014).
[14] W. Li, J. Carrete, N. A. Katcho, and N. Mingo, Comput. Phys. Commun. **185**, 1747 (2014).
[15] A. Togo, L. Chaput, and I. Tanaka, Phys. Rev. B **91**, 094306 (2015).
[16] T. Tadano and S. Tsuneyuki, Phys. Rev. B **92**, 054301 (2015).
[17] A. Cepellotti and N. Marzari, Phys. Rev. X **6**, 041013 (2016).
[18] L. Lindsay, Nanosc. Microsc. Therm. **20**, 67 (2016).
[19] G. Fugallo and L. Colombo, Phys. Scr. **93**, 043002 (2018).
[20] H. Aramberri, R. Rurali, and J. Íñiguez, Phys. Rev. B **96**, 195201 (2017).
[21] S. M. Antao, I. Hassan, J. Wang, P. L. Lee, and B. H. Toby, Can. Mineral. **46**, 1501 (2008).

[22] J. J. Pluth, J. V. Smith, and J. Faber Jr, J. Appl. Phys. **57**, 1045 (1985).
[23] H. Kanamori, N. Fujii, and H. Mizutani, J. Geophys. Res. **73**, 595 (1968).
[24] M. Kunugi, N. Soga, H. Sawa, and A. Konishi, J. Am. Ceram. Soc. **55**, 580 (1972).
[25] A. Togo, "Phonopy", https://github.com/atztogo/phonopy.
[26] A. Togo, "Phono3py", https://github.com/atztogo/phono3py.
[27] G. P. Srivastava, *Physics of phonons* (CRC Press, New York, 1990).
[28] A. Togo and I. Tanaka, Scr. Mater. **108**, 1 (2015).
[29] S.-i. Tamura, Phys. Rev. B **27**, 858 (1983).
[30] P. Bridgman, Am. J. Sci. **7**, 81 (1924).
[31] O. Alm and G. Bäckström, J. Phys. Chem. Solids **35**, 421 (1974).
[32] G. A. Slack, Solid State Phys. **34**, 1 (1979).
[33] D. Gerlich and P. Andersson, J. Phys. C **15**, 5211 (1982).
[34] R. G. Ross, P. Andersson, B. Sundqvist, and G. Bäckström, Rep. Prog. Phys. **47**, 1347 (1984).
[35] L. Chaput, A. Togo, I. Tanaka, and G. Hug, Phys. Rev. B **84**, 094302 (2011).
[36] R. M. Pick, M. H. Cohen, and R. M. Martin, Phys. Rev. B **1**, 910 (1970).
[37] X. Gonze, J.-C. Charlier, D. C. Allan, and M. P. Teter, Phys. Rev. B **50**, 13035 (1994).
[38] X. Gonze and C. Lee, Phys. Rev. B **55**, 10355 (1997).
[39] Y. Wang, J. J. Wang, W. Y. Wang, Z. G. Mei, S. L. Shang, L. Q. Chen, and Z. K. Liu, J. Phys.: Condens. Matter **22**, 202201 (2010).
[40] P. E. Blöchl, Phys. Rev. B **50**, 17953 (1994).
[41] G. Kresse, J. Non-Cryst. Solids **193**, 222 (1995).
[42] G. Kresse and J. Furthmüller, Comput. Mater. Sci. **6**, 15 (1996).
[43] G. Kresse and D. Joubert, Phys. Rev. B **59**, 1758 (1999).
[44] J. P. Perdew, A. Ruzsinszky, G. I. Csonka, O. A. Vydrov, G. E. Scuseria, L. A. Constantin, X. Zhou, and K. Burke, Phys. Rev. Lett. **100**, 136406 (2008).
[45] M. Gajdoš, K. Hummer, G. Kresse, J. Furthmüller, and F. Bechstedt, Phys. Rev. B **73**, 045112 (2006).
[46] X. Wu, D. Vanderbilt, and D. R. Hamann, Phys. Rev. B **72**, 035105 (2005).
[47] J. P. Perdew, K. Burke, and M. Ernzerhof, Phys. Rev. Lett. **77**, 3865 (1996).
[48] C. Adamo and V. Barone, J. Chem. Phys. **110**, 6158 (1999).
[49] J. Linnera and A. J. Karttunen, Phys. Rev. B **96**, 014304 (2017).
[50] D. M. Ceperley and B. J. Alder, Phys. Rev. Lett. **45**, 566 (1980).
[51] J. P. Perdew and A. Zunger, Phys. Rev. B **23**, 5048 (1981).
[52] M. I. Aroyo, D. Orobengoa, G. de la Flor, E. S. Tasci, J. M. Perez-Mato, and H. Wondratschek, Acta Crystallogr. Sect. A **70**, 126 (2014).
[53] B. Dorner, H. Grimm, and H. Rzany, J. Phys.: Condens. Matter **13**, 6607 (1980).
[54] D. Strauch and B. Dorner, J. Phys.: Condens. Matter **5**, 6149 (1993).
[55] I. P. Swainson and M. T. Dove, J. Phys.: Condens. Matter **7**, 1771 (1995).
[56] M. T. Dove, M. J. Harris, A. C. Hannon, J. M. Parker, I. P. Swainson, and M. Gambhir, Phys. Rev. Lett. **78**, 1070 (1997).
[57] B. Wehinger, A. Bosak, K. Refson, A. Mirone, A. Chumakov, and M. Krisch, J. Phys.: Condens. Matter **27**, 305401 (2015).
[58] A. P. Giddy, M. T. Dove, G. S. Pawley, and V. Heine, Acta Crystallogr. Sect. A **49**, 697 (1993).
[59] M. T. Dove, K. O. Trachenko, M. G. Tucker, and D. A. Keen, Rev. Mineral. Geochem. **39**, 1 (2000).
[60] S. A. Wells, M. T. Dove, M. G. Tucker, and K. O. Trachenko, J. Phys.: Condens. Matter **14**, 4645 (2002).